COMMUNICATION

Structured Metal Film as a Perfect Absorber

*Xiang Xiong, Shang-Chi Jiang, Yu-Hui Hu, Ru-Wen Peng, and Mu Wang**

The fact that a flat metal surface can be used as a reflector (mirror) has been known for thousands of years. Nowadays a continuous metal film can be regarded as a reflector to light (more than 99% reflection and less than 0.1% transmission for metal film a few tens of nanometers in thickness, for example) over a very broad band of frequency. However, when microstructures are introduced to metallic thin films, even in the scenario that the film remains continuous, the situation can be different. In fact, the interaction of electromagnetic waves with a subwavelength metallic microstructure has attracted much attention in recent decades due to the novel physical properties involved. With specially designed sub-wavelength metallic structures, it is possible to achieve novel electromagnetic properties such as negative refractive index,[1,2] ultrahigh spatial resolution beyond the diffraction limit,[3,4] invisibility cloaking,[5–7] and optical magnetics.[8] Among the massive amount of research in this area, one of the intensively studied subjects is the design of metamaterial absorbers,[9–14] which neither reflect nor transmit incident light, and in which the energy of the incident light is mostly absorbed. This function makes the microstructure promising for applications in photovoltaic solar cell,[15] microbolometers,[16] spatial imaging,[17] and high sensitive detectors,[18,19] etc..

The absorber was proposed for the first time by Landy et al.[9] with a trilayer structure with absorbance greater than 88%. Since then, different structures have been designed for frequencies ranging from microwave,[20–22] terahertz (THz),[10,23,24] infrared,[17,25] and even optical frequencies.[14] The most commonly used design is the trilayer approach. The top layer is a patterned metallic thin film and is separated from the bottom metallic film by a dielectric interlayer.[12,17,25] The physical mechanism of the absorption effect has been ascribed to the excitation of localized electromagnetic resonances. The existence of magnetic resonance is characterized by the antiparallel surface currents excited on the two separated metallic layers.[14] Due to heat generation in the absorber, as a detector, an absorber is challenged by problems such as ultrafast heating, surface melting, and reshaping.[26–28] In conventional design, despite that the metal itself is a good thermal conductor, the dielectric layer sandwiched between the metallic layers hinders the efficient thermal dissipation.

In this communication, we report a new type of absorber constructed with an assembly of four-tined fish-spear-like resonators (FFRs). With the two-photon polymerization process,[29,30]

Dr. X. Xiong, S.-C. Jiang, Y.-H. Hu, Prof. R.-W. Peng, Prof. M. Wang
National Laboratory of Solid State Microstructures
& Department of Physics
Nanjing University
Nanjing 210093, China
E-mail: muwang@nju.edu.cn

we fabricate such a three-dimensional (3D) microstructure and then coat it with a layer of continuous gold film, 35 nm in thickness. The operating frequency of the FFR absorber is in the mid-infrared range (1000–2000 cm⁻¹) and an absorbance of 90% has been experimentally realized. In our design, the resonance occurs in the space between the tines of the FFR instead of between two metallic layers separated by the dielectric interlayer. The continuous metallic thin film covering both the FFR array and the substrate surface plays the role of a perfect thermal and electric conductor, which is, in fact, desired in many applications.[14,31]

The elementary building block of the FFR absorber consists of two cross-standing, identical U-shaped resonators.[32–34] A continuous gold film, 35 nm in thickness, covers the FFR structure, as illustrated in **Figure 1**a. Two U-shaped microstructures stand along the x- and y-directions respectively and the openings of the tines both point upward in z-direction. An array of the unit is constructed in a simple square lattice with lattice constant L. The interior structure of the FFR is illustrated in Figure 1b, and it is made by two-photon polymerization in UV-curable photoresists. The optical properties are measured by propagating the x-polarized incident light in the $-z$-direction. Due to the four-fold symmetry of the FFR unit, the transmission and reflection coefficients are polarization-independent. Before the experiments, commercial software based on the finite-difference time-domain method is applied to simulate the physical properties of the FFR array. The permittivity of gold in the infrared regime is calculated based on the Drude model, $\varepsilon(\omega) = 1 - \omega_p^2/(\omega^2 + i\omega_\tau\omega)$, where ω_p is the plasma frequency and ω_τ is the damping constant. For gold, these characteristic frequencies are taken as $\omega_p = 2\pi(2.175 \times 10^{15})$ s⁻¹, and $\omega_\tau = 6\pi(6.5 \times 10^{12})$ s⁻¹.[35,36] The substrate is a glass plate and the U-shaped interior is the IP-L photoresist with a refractive index of 1.5.[37]
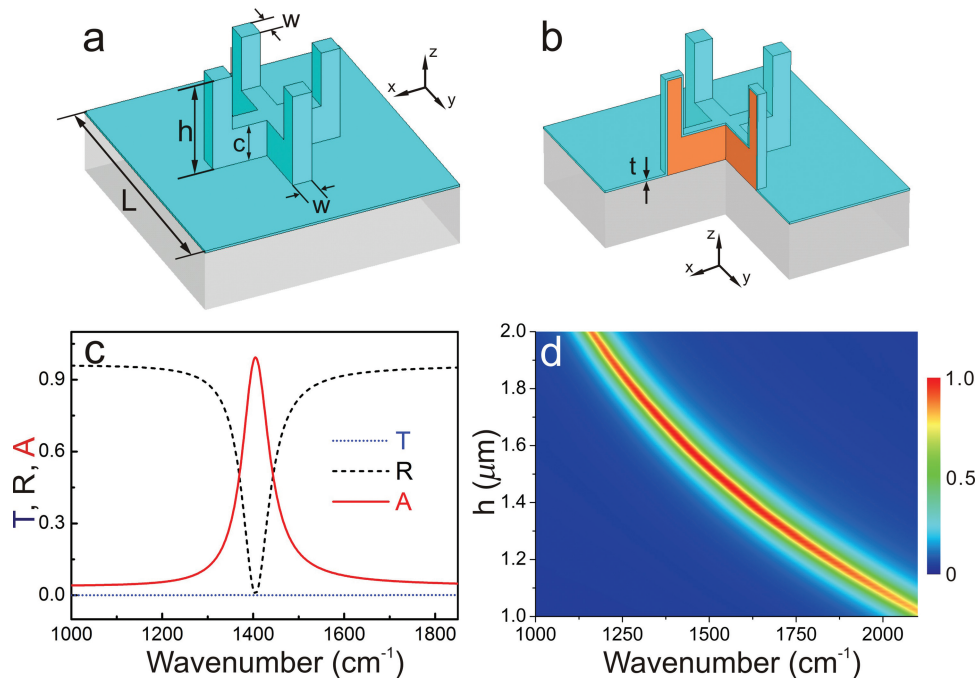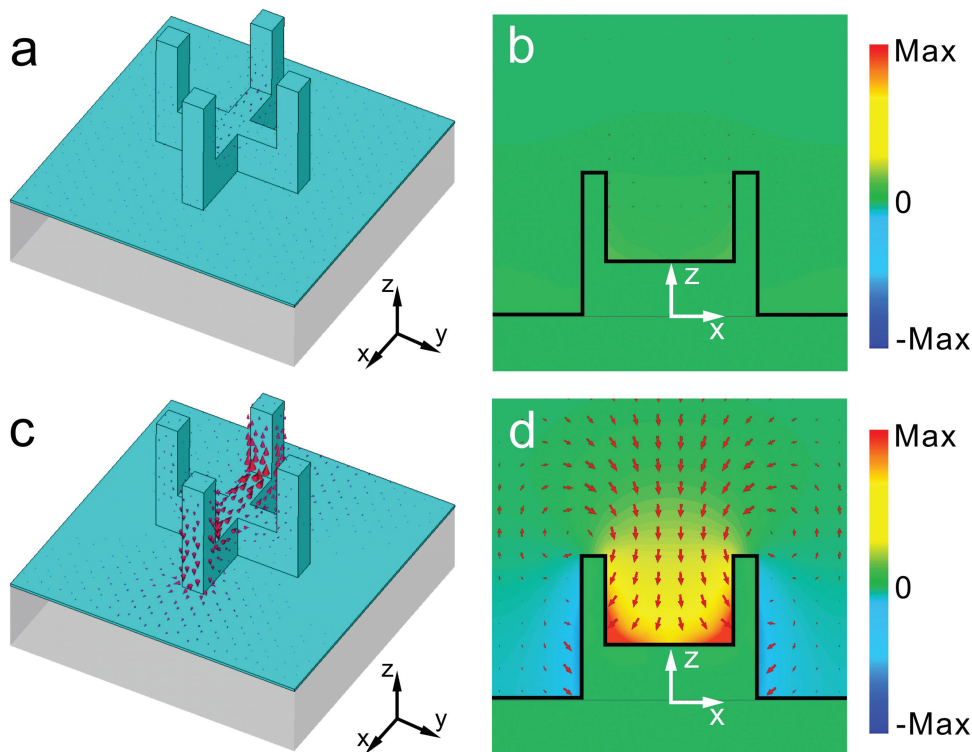
The scattering parameter (S-parameter) is a square matrix describing the electrical behavior of a linear system undergoing various steady-state electrical stimuli, which can be obtained by simulation.[38] Many important parameters can be derived by the elements in the S-parameter matrix. For example, the reflection is defined as $R = |S_{11}|^2$, and the transmission is defined as $T = |S_{21}|^2$. The absorbance A is obtained by $A = 1 - R - T = 1 - |S_{11}|^2 - |S_{21}|^2$.[9] In Figure 1c, the reflection possesses a clear resonance at 1400 cm⁻¹, while the transmission remains zero (less than 5‰) throughout. The absorbance reaches 99.3% at 1400 cm⁻¹, which is nearly the complete absorption. In Figure 1d, we change the height of the FFR (h) while keeping the rest of the geometrical parameters constant, and calculate the absorbance of the array as a function of the frequency of the incident light. It follows that, by shrinking the height of the FFR, the maximum absorbance shifts to a higher frequency. More than 95% absorbance can be achieved when h varies from 1.3 μm to 1.8 μm, where the wavenumber of the maximum absorbance varies from 1300 cm⁻¹ to 1700 cm⁻¹.

To understand the mechanism of absorption, the induced surface electric current (**Figure 2**a and c) on the FFR and the

Makrials
Views
www.MaterialsViews.com

ADVANCED
MATERIALS
www.advmat.de

COMMUNICATION

Figure 1. a) The morphology of an FFR unit with structural parameters: $L = 4$ μm, $h = 1.6$ μm, $c = 0.6$ μm, and $w = 0.3$ μm. The separation of the facing tines within the U-shape is 1.7 μm. b) A graph to illustrate the interior of an FFR unit cell. The polymer FFR is covered with a gold layer of thickness t. (c) The calculated transmission (T), reflection (R) and absorbance (A) for the scenario of tine height $h = 1.6$ μm. d) The absorbance spectrum as a function of wavenumber with different tine heights (h).

Figure 2. a) The calculated induced surface electric-current density on an FFR unit cell at 1800 cm^{-1}, which is far away from the resonance frequency. b) The calculated distribution of the y-component of the magnetic field at cross section $y = 0$ at 1800 cm^{-1}. c) The calculated induced surface electric-current density on an FFR unit cell at 1400 cm^{-1}, which is exactly the resonance frequency of the FFR. d) The calculated distribution of the y-component of the magnetic fields at cross section $y = 0$ at 1400 cm^{-1}. The red arrows in (b) (most arrows have vanished here) and (d) represent the Poynting vector.
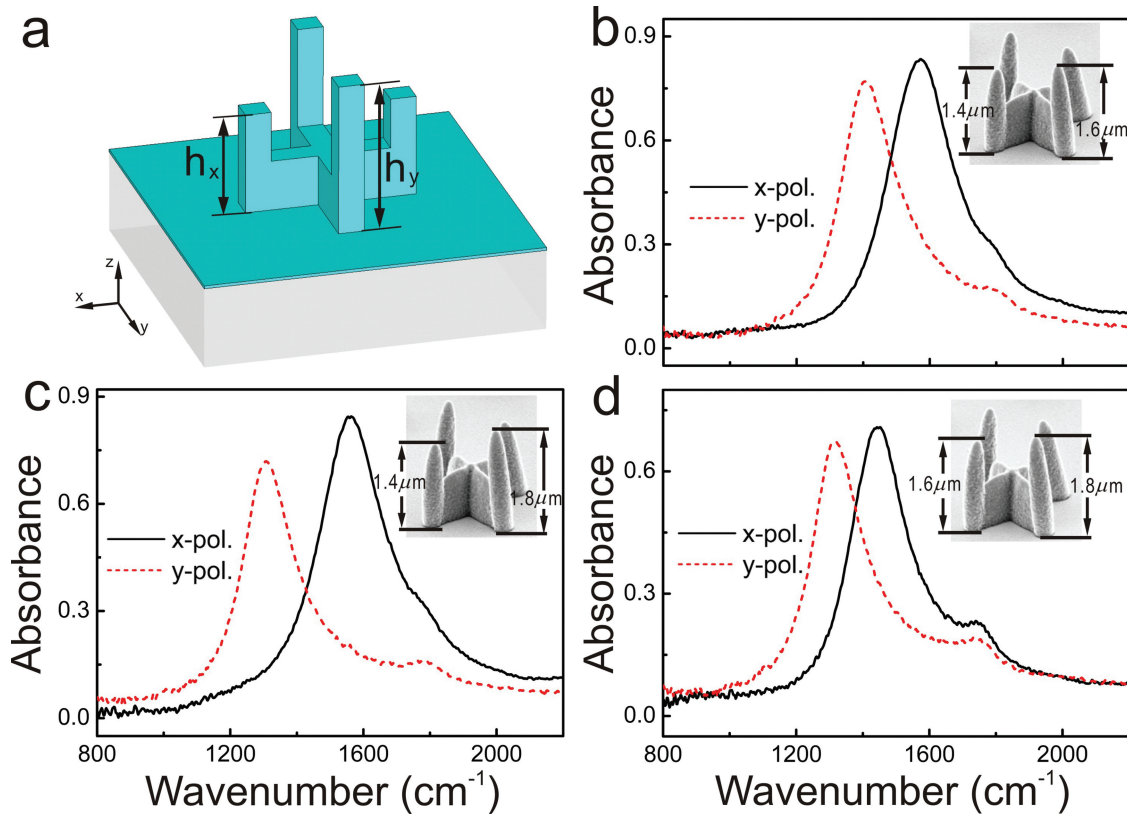
Figure 3. a) The field-emission scanning electron microscopy (FESEM) image of the FFRs. The scale bar represents 5 μm. The measured transmission (*T*), reflection (*R*) and absorbance (*A*) for the scenarios of: b) $h = 1.4$ μm, c) $h = 1.6$ μm, and d) $h = 1.8$ μm, respectively. The insets in (b)–(d) illustrate the corresponding FESEM images of the FFR units in each scenario, where the height of the tines varies.

induced magnetic field (Figure 2b,d) are calculated, respectively. The geometrical parameters of the FFR here are exactly the same as that in Figure 1a. The *y*-component of the magnetic field is collected at each point of the *x–z* plane at *y* = 0. Figure 2a shows the induced surface electric current at 1800 cm^{-1} for *x*-polarized incidence, which is far away from the absorption frequency. In this scenario, the reflection is 95%, and the absorbance is 5%, and the induced surface electric current can hardly be detected. At this frequency, most of the incident light has been reflected. Meanwhile, the electromagnetic power propagating along the −*z*- and *z*-directions cancel out and the Poynting vector in the *x–z* plane virtually approaches zero. Therefore in Figure 2b, the red arrows representing the distribution of Poynting vector in the *x–z* plane, approach zero.

The situation differs significantly at 1400 cm^{-1} where absorption occurs. At 1400 cm^{-1}, the incident light is *x*-polarized, the induced surface electric current flows along the −*x*-direction on the surface of the U-shaped structure standing along the *x*-direction. The surface electric current tends to form a loop in the *x–z* plane. According to Ampere's law, an effective magnetic field is generated in the *y*-direction. The induced magnetic field is shown between the two tines in Figure 2d. The plot of the Poynting vector indicates that the electromagnetic energy propagates downward in the *z*-direction and then whirls to the opening of the FFR, forming vortices near the

ends of the FFR tines (Figure 2d). The energy of the incident light is trapped between the tines, and is finally absorbed. In this scenario, reflection is suppressed.

To verify the above calculations, we fabricated an array of FFRs with a 3D nanofabrication approach based on two-photon polymerization. **Figure 3**a shows a field-emission scanning electron microscopy (FESEM) image of the fabricated FFR array. Three sets of FFR assembly are fabricated with $h = 1.4$ μm, 1.6 μm, and 1.8 μm, respectively, as indicated in the insets of Figures 3b–d. Fourier transform infrared (FTIR) microscopy is applied to characterize the optical properties of the structures. The FTIR spectroscopy measurements confirm that the absorption frequency can be tuned with different height of FFR. For the scenario that the height of the FFR is 1.4 μm, as indicated in Figure 3b, the absorbance reaches 90% at 1600 cm^{-1}, where the reflection reaches a minimum. When the height of the FFR increases, the magnetic resonance shifts to a lower frequency. The impedance of the FFR array mismatches that of free space,[9] and more incident energy is reflected back. As shown in Figure 3c,d, the absorbance reaches 83% at 1430 cm^{-1} and 71% at 1300 cm^{-1}, respectively. The measured transmission is less than 2‰ at the absorption frequency. The measurements are in good agreement with simulations. In Figure 3, the FFR array is four-fold symmetrical, so the absorption is independent of the polarization of the incident light. It should be noted that,

Materials
Views
www.MaterialsViews.com

ADVANCED
MATERIALS
www.advmat.de

COMMUNICATION

Figure 4. a) The illustration to show the FFR unit with different tine heights in the *x*- and *y*-directions. b–d) The measured absorbance for the scenarios of: b) $h_x = 1.4$ μm, $h_y = 1.6$ μm; c) $h_x = 1.4$ μm, $h_y = 1.8$ μm; and d) $h_x = 1.6$ μm, $h_y = 1.8$ μm, respectively. The black solid lines correspond to the absorbance for the *x*-polarized incidence, and the red (grey) dashed lines correspond to the absorbance for the *y*-polarized incidence. The insets in (b)–(d) illustrate the FESEM images of the FFR units with different h_x and h_y combinations.
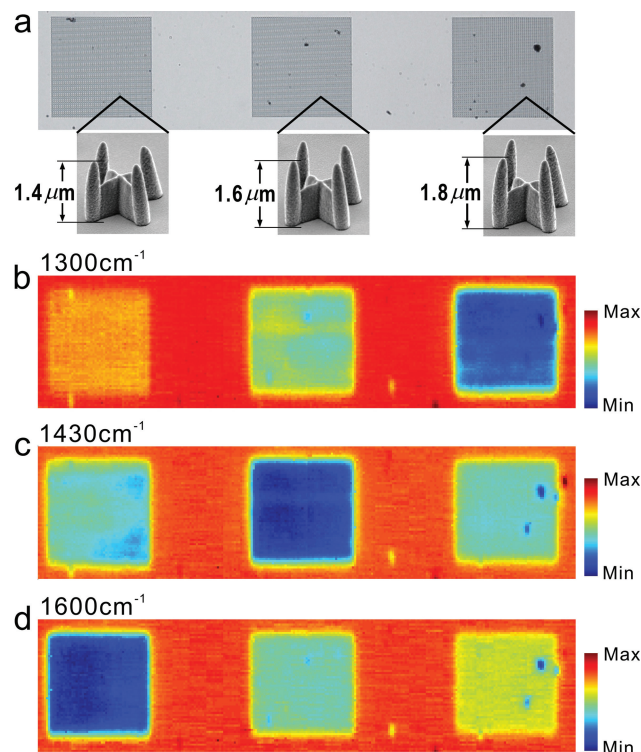
in the absorbance spectra shown in Figure 3, the shorter-wavenumber-end is slightly lower than the longer-wavenumber-end. Calculations indicate that this effect can be ascribed to the limitation of the fabrication precision in fabricating the FFRs, since the fluctuation of tine height by several tens of nanometers can generate noticeable change of absorbance at the two ends.

The polarization-independent feature shown in Figure 1a exists only in the situation of identical-tine-height-geometry. If the height of the tines of the FFR deviates, the situation is different. As illustrated in **Figure 4**a, suppose that the height of the tines standing along the *x*-axis is h_x, while the height of those along the *y*-axis is h_y, and h_y is designed to be higher than h_x. We fabricate three sets of FFR arrays with different combination of h_x and h_y. In Figure 4b, we have $h_x = 1.4$ μm, $h_y = 1.6$ μm; in Figure 4c, $h_x = 1.4$ μm, $h_y = 1.8$ μm; while in Figure 4d, $h_x = 1.6$ μm, $h_y = 1.8$ μm, respectively. It follows that the frequency corresponding to the maximum absorbance varies when the polarization of the incident light is changed. In Figure 4b ($h_x = 1.4$ μm, $h_y = 1.6$ μm), the maximum absorbance occurs at 1600 cm^{-1} for *x*-polarized incidence, and at 1430 cm^{-1} for *y*-polarized incidence, respectively. In Figure 4c ($h_x = 1.4$ μm, $h_y = 1.8$ μm), the maximum absorbance occurs at 1600 cm^{-1} for *x*-polarized incidence, and at 1300 cm^{-1} for *y*-polarized incidence, respectively. For the $h_x = 1.6$ μm, $h_y = 1.8$ μm in Figure 4d, the maximum absorbance frequency is at 1430 cm^{-1} for *x*-polarized incidence and at 1300 cm^{-1}

for *y*-polarized incidence. This result suggests that by introducing different height of the tines in *x*- and *y*-orientated U-structures, with the same arrays of FFRs, it is possible to switch the absorption at two frequencies by changing the polarization of the incident light.

In the fabrication process, it is, in practice, difficult to keep the height of the two tines within one U-shaped nanostructure exactly identical. The deviation of the tine height in the U-patterns is responsible for the formation of the small shoulder appearing on the right side of the main resonant peak, as shown in Figure 3 and 4. At the shoulder site, the induced surface electric current resonates in an asymmetrical mode.
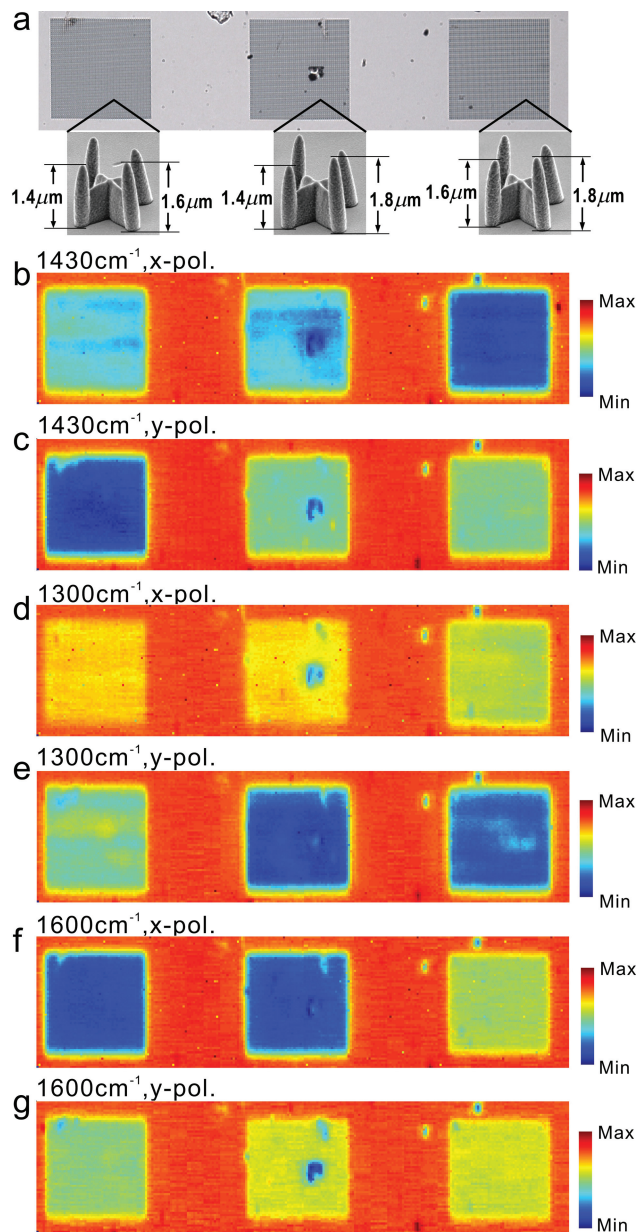
We intentionally fabricate FFR arrays with different tine heights and compare the absorption efficiency at different frequencies with the focus plane array (FPA) imaging system. The results are shown in **Figure 5**. Each array is 200 μm × 200 μm in size, and was fabricated on the same glass substrate, and each was placed in parallel, as illustrated in Figure 3a. The space between each array is the substrate covered with a gold layer. The structural details of the unit cell in each array are shown by the insets in Figure 5a. Figure 5b–d show the FPA imaging at different frequencies, where the red color (bright) indicates that more energy has been reflected and detected by the FPA detector; in other words, the absorption is weak; the blue color (dark) indicates that less reflection energy is detected by the FPA detector, and the absorption is strong. Figure 5b shows the

Figure 5. a) The micrograph of FFR arrays with different heights *h*. The dimension of each array is 200 μm × 200 μm. In between each array is the flat glass substrate covered with a gold layer. The insets show the FESEM images of the FFR unit in each array, respectively. The FPA images of that shown in (a) have been grabbed at different wavenumbers: b) 1300 cm⁻¹; c) 1430 cm⁻¹; and d) 1600 cm⁻¹. In (b)–(d) the red color (bright) indicates that more energy has been reflected from the surface and is hence detected by the FPA detector. In these places the absorption is weak. The blue color (dark) indicates that little reflection energy is detected by the FPA detector, indicating that the local absorption is strong.

scenario grabbed at 1300 cm⁻¹, the FFR array (right) with *h* = 1.8 μm shows the strongest absorption, while the FFR arrays with *h* = 1.6 μm (middle) and *h* = 1.4 μm (left) illustrate weaker and weakest absorption, respectively. At 1430 cm⁻¹, as indicated in Figure 5c, the middle array (*h* = 1.6 μm) shows the strongest absorption and the other two arrays show weaker absorption. At 1600 cm⁻¹, as demonstrated in Figure 5d, the leftmost array (*h* = 1.4 μm) possesses the strongest absorption. Therefore, we conclude from the FPA measurements that the frequency with the strongest absorption depends on the height of the tines in FFR. By shrinking the height of the FFR, *h*, the frequency of the maximum absorbance shifts to the higher frequency.

In order to demonstrate the function of the polarization-dependent absorption, we fabricate FFR arrays with different tine height in the *x*- and *y*-directions. In **Figure 6**, three arrays of FFR arrays have been fabricated with different combination of the tine height in the *x*- and *y*-directions. In Figure 6a, the left array possesses h_x = 1.4 μm, and h_y = 1.6 μm; the array in the middle part corresponds to h_x = 1.4 μm and h_y = 1.8 μm; and the rightmost array is constructed with h_x = 1.6 μm and h_y = 1.8 μm. The detailed morphology of the building unit in each array is illustrated in the insets of Figure 6a. FPA imaging at 1430 cm⁻¹ with *x*-polarized incidence is illustrated in

Figure 6. a) Microscopy image of the FFR arrays with different h_x and h_y combinations. The dimensions of each array are 200 μm × 200 μm. In between each array is the flat glass substrate covered with a gold layer. The insets show the FESEM micrograph of the FFR unit in each array, respectively. The FPA images of the same region as that shown in (a) are grabbed at different wavenumbers: b,c) 1430 cm⁻¹, with *x*/*y*-polarized incidence; d,e) 1300 cm⁻¹, with *x*/*y*-polarized incidence; f,g) 1600 cm⁻¹, with *x*/*y*-polarized incidence, respectively.

Figure 6b. At 1430 cm⁻¹, for *x*-polarized incidence, the FFR arrays with h_x = 1.6 μm shows the strongest absorption, whereas the arrays at leftmost and in the middle part (with h_x = 1.4 μm) show much weaker absorption. At the same frequency, by changing the polarization of the incident light to *y*-polarization, as indicated in Figure 6c, the left array with h_y = 1.6 μm shows the strong absorption, whereas the middle and the rightmost arrays (h_y = 1.8 μm) show much weaker absorption. At

1300 cm^{-1} and with x-polarized incidence, the three FFR arrays with h_x = 1.4 μm and 1.6 μm, respectively, show much weaker absorption. Yet at the same frequency, for y-polarized incidence, the middle and the leftmost arrays (h_y = 1.8 μm) show stronger absorption,as illustrated in Figure 6e. At 1600 cm^{-1} and x-polarized incidence, FFR arrays with h_y = 1.4 μm show strong absorption. At 1600 cm^{-1} and y-polarized incidence, however, all the arrays in Figure 6g (with h_y = 1.6 μm and 1.8 μm, respectively) show much weaker absorption. Therefore, Figure 6 confirms that the FFRs with different h_x and h_y have different absorption frequencies for x- and y-polarized incidence, respectively. The frequency of the polarization-dependent absorption is selected with the tine heights in x- and y-directions.

For a flat gold film, 35 nm in thickness, we calculated its transmission and reflection in the band 30–300 THz. It turns out that both the reflection and transmission are kept as a constant, and the reflection is more than 99% and the transmission is less than 0.1%. This means that a flat, unstructured metal film merely plays the role of a perfect reflector (as illustrated by the red regions surrounding each arrays in Figures 5 and 6). By introducing FFRs, however, the situation is changed dramatically. As that demonstrated above, FFRs make the surface a perfect absorber at certain frequency, and the absorption frequency depends on the structural parameters of the FFR. Comparing with previously reported absorbers,[9,24–27] in our FFR structure, the resonance occurs between the tines of the spears instead of in the dielectric interlayer sandwiched between two metallic layers. Therefore, for the FFR structure, once the heat is generated, it will not be accumulated locally to trigger the possible damages to the device.[14] In addition, the continuous metallic coating also makes the FFR array electrically conductive, which may have potential applications for device design.[31] The other advantage of our structure is that the materials applied to construct the FFR are not strictly selective. In fact, in the mid-IR range, we have tested the materials with different refractive index with n_{sub} and n_{but} varying from 1 to 10 in modeling of the substrate and the interior of FFR. It turns out that the transmission and reflection spectra are identical in all these scenarios, suggesting that the material of the substrate and of the interior of FFR can be selected with large freedom. This feature makes it much easier to apply our FFR structure as a coating on optical surfaces for sensor applications.

In conclusion, we demonstrate for the first time the designing, fabrication and characterization of the FFR structure made of two cross-standing U-shaped resonators. The structures have been fabricated with two-photon polymerization process. The operating frequency of the FFR absorber is in the mid-IR range (1000–2000 cm^{-1}) and an absorbance of 90% has been experimentally realized. In our system, resonance occurs in the space between the tines of the FFR instead of inside the dielectric interlayer sandwiched by two metallic layers, so the heat generated in FFR can be more easily dissipated.

Experimental Section

Two-Photon Polymerization Micro-fabrication: A Nanoscribe photonic professional two-photon lithography system was applied in the fabrication. The lithography system focuses a femtosecond laser beam to a diffraction-limited spot where it catalyzes a chemical change in the photoresist (IP-L). By controlling the position of the laser focal spot, 3D structures can be made. During the fabrication, a glass substrate with a thickness of 170 μm (Menzel-Glaser) was used as the substrate. The IP-L two-photon negative photoresist was placed at the beam focus and the FFR structure was written by controlling the movement of the glass substrate. The exposed photoresist was then developed and only the FFR structure bonded to the glass substrate remained. The FFR structures were then coated with 35 nm of thick gold film by magnetron sputtering. In this way, an FFR array coated with gold film was generated.

FTIR Spectroscopy Measurements: FTIR microscopy (Bruker Hyperion 3000) associated with the Bruker Vertex 70V FTIR Spectrometer was used to characterize the optical property of the fabricated structures. A pair of mid-IR ZnSe polarizers is applied to control the polarization of the incident light and analyze the transmitted light. A focus plane array (FPA) imaging system (Hyperion 3000, Bruker) was used to collect the IR spatial image. The FPA image was grabbed at a center wavenumber, with an integral width of 10 cm^{-1}.

[1] R. A. Shelby, D. R. Smith, S. Schultz, *Science* **2001**, *292*, 77.
[2] D. R. Smith, J. B. Pendry, M. C. K. Wiltshire, *Science* **2004**, *305*, 788.
[3] N. Fang, H. Lee, C. Sun, X. Zhang, *Science* **2005**, *308*, 534.
[4] N. Fang, X. Zhang, *Appl. Phys. Lett.* **2003**, *82*, 161.
[5] J. B. Pendry, D. Schurig, D. R. Smith, *Science* **2006**, *312*, 1780.
[6] W. S. Cai, U. K. Chettiar, A. V. Kildishev, V. M. Shalaev, *Nat. Photonics* **2007**, *1*, 224.
[7] F. Zhou, Y. J. Bao, W. Cao, C. T. Stuart, J. Q. Gu, W. L. Zhang, C. Sun, *Sci. Rep.* **2011**, *1*, 78.
[8] Z. M. Huang, J. Q. Xue, Y. Hou, J. H. Chu, D. H. Zhang, *Phys. Rev. B* **2006**, *74*, 193105.
[9] N. I. Landy, S. Sajuyigbe, J. J. Mock, D. R. Smith, W. J. Padilla, *Phys. Rev. Lett.* **2008**, *100*, 207402.
[10] N. I. Landy, C. M. Bingham, T. Tyler, N. Jokerst, D. R. Smith, W. J. Padilla, *Phys. Rev. B* **2009**, *79*, 125104.
[11] Y. Avitzour, Y. A. Urzhumov, G. Shvets, *Phys. Rev. B* **2009**, *79*, 045131.
[12] K. Aydin, V. E. Ferry, R. M. Briggs, H. A. Atwater, *Nat. Commun.* **2011**, *2*, 517.
[13] C. M. Watts, X. L. Liu, W. J. Padilla, *Adv. Mater.* **2012**, *24*, OP98.
[14] J. M. Hao, J. Wang, X. L. Liu, W. J. Padilla, L. Zhou, M. Qiu, *Appl. Phys. Lett.* **2010**, *96*, 251104.
[15] Y. Wang, T. Sun, T. Paudel, Y. Zhang, Z. Ren, K. Kempa, *Nano Lett.* **2012**, *12*, 440.
[16] T. Maier, H. Brueckl, *Opt. Lett.* **2009**, *34*, 3012.
[17] X. L. Liu, T. Starr, A. F. Starr, W. J. Padilla, *Phys. Rev. Lett.* **2010**, *104*, 207403.
[18] N. Liu, M. Mesch, T. Weiss, M. Hentschel, H. Giessen, *Nano Lett.* **2010**, *10*, 2342.
[19] D. Shrekenhamer, W. R. Xu, S. Venkatesh, D. Schurig, S. Sonkusale, W. J. Padilla, *Phys. Rev. Lett.* **2012**, *109*, 177401.
[20] B. N. Wang, T. Koschny, C. M. Soukoulis, *Phys. Rev. B* **2009**, *80*, 033108.

[21] K. B. Alici, F. Bilotti, L. Vegni, E. Ozbay, *J. Appl. Phys.* **2010**, *108*, 083113.

[22] Y. Z. Cheng, H. L. Yang, *J. Appl. Phys.* **2010**, *108*, 034906.

[23] D. Y. Shchegolkov, A. K. Azad, J. F. O'Hara, E. I. Simakov, *Phys. Rev. B* **2010**, *82*, 205117.

[24] J. Grant, Y. Ma, S. Saha, A. Khalid, D. R. S. Cumming, *Opt. Lett.* **2011**, *36*, 3476.

[25] Z. H. Jiang, S. Yun, F. Toor, D. H. Werner, T. S. Mayer, *ACS Nano* **2011**, *5*, 4641.

[26] J. Wang, Y. T. Chen, X. Chen, J. M. Hao, M. Yan, M. Qiu, *Opt. Express* **2011**, *19*, 14726.

[27] X. Chen, Y. T. Chen, M. Yan, M. Qiu, *ACS Nano* **2012**, *6*, 2550.

[28] H. B. Sun, T. Tanaka, K. Takada, S. Kawata, *Appl. Phys. Lett.* **2001**, *79*, 1411.

[29] M. Thiel, M. S. Rill, G. von Freymann, M. Wegener, *Adv. Mater.* **2009**, *21*, 4680.

[30] S. Kawata, H. B. Sun, T. Tanaka, K. Takada, *Nature* **2001**, *412*, 697.

[31] H.-T. Chen, W. J. Padilla, J. M. O. Zide, A. C. Gossard, A. J. Taylor, R. D. Averitt, *Nature* **2006**, *444*, 597.

[32] X. Xiong, W. H. Sun, Y. J. Bao, R. W. Peng, M. Wang, C. Sun, X. Lu, J. Shao, Z. F. Li, N. B. Ming, *Phys. Rev. B* **2009**, *80*, 201105.

[33] X. Xiong, W. H. Sun, Y. J. Bao, M. Wang, R. W. Peng, C. Sun, X. Lu, J. Shao, Z. F. Li, N. B. Ming, *Phys. Rev. B* **2010**, *81*, 075119.

[34] X. Xiong, S. C. Jiang, Y. H. Hu, J. M. Zhao, Y. J. Feng, R. W. Peng, M. Wang, *AIP Adv.* **2012**, *2*, 041413.

[35] N. Liu, L. Langguth, T. Weiss, J. Kastel, M. Fleischhauer, T. Pfau, H. Giessen, *Nat. Mater.* **2009**, *8*, 758.

[36] G. Dolling, C. Enkrich, M. Wegener, C. M. Soukoulis, S. Linden, *Science* **2006**, *312*, 892.

[37] M. Schroeder, M. Buelters, C. von Kopylow, R. B. Bergmann, *J. Eur. Opt. Soc, Rapid Publ.* **2012**, *7*, 12027.

[38] D. R. Smith, S. Schultz, P. Markos, C. M. Soukoulis, *Phys. Rev. B* **2002**, *65*, 195104.